IEEE/ASME Transactions on Mechatronics, Vol. 23, No. 6, pp. 2963-2967, December 2018

A 150 000-r/min Bearingless Slice Motor

P. Püntener,
M. Schuck,
D. Steinert,
T. Nussbaumer,
J. W. Kolar

A 150 000 rpm Bearingless Slice Motor

Pascal Puentener, *Student Member*, *IEEE*, Marcel Schuck, *Member*, *IEEE*, Daniel Steinert, *Student Member*, *IEEE*, Thomas Nussbaumer, *Member*, *IEEE*, and Johann W. Kolar, *Fellow*, *IEEE*

***Abstract*—In this paper, the design and operating principle of a slotless bearingless slice motor for high rotational speeds is presented. The performance of the proposed concept is evaluated using an experimental prototype. Measurement results demonstrate a stable dynamic behavior during acceleration and an achievable rotational speed of 150 000 rpm, which is, to the knowledge of the authors, the highest rotational speed attained by a bearingless slice motor to date. The system performance is outlined at its maximum speed and power loss measurements are carried out over the entire speed range.**

***Index Terms*—bearingless motor, slice motor, high rotational speed, slotless, toroidal winding**

I. Introduction

RECENT years have shown a trend in electrical drive systems toward high power densities achieved by increased rotational speeds. Magnetically levitated motors are ideally suited for high speed applications due to their lack of mechanical bearings and the associated friction losses. One of such motors has been reported to operate at rotational speeds as high as 400 000 rpm [1]. It consists of a cylindrical rotor and two radial as well as one axial magnetic bearing unit.

In this paper, a bearingless slice motor is presented that consists of a single magnetic bearing unit integrated into the motor for stabilization of the rotor in radial direction. The remaining three degrees of freedom, namely axial displacement and tilting, are stabilized passively by restoring reluctance forces caused by the deflection of the rotor [2], [3], [4]. To achieve passive stability in the tilting direction, the diameter of the rotor is required to be significantly larger than its height. The slice motor topology yields a more compact and simple construction and is already used in industrial applications, such as high-purity mixers [5], pumps [6], turbocompressors and artificial hearts [7], [8].

As the stator of such a machine is usually slotted, fluctuations of the magnetic field exist, which cause significant losses at high rotational speeds [9]. To reduce these losses, a slotless stator is advantageous and has been explored in [10], [11]. A schematic view of the resulting motor topology is shown in Fig. 1. The highest rotational speed achieved by a bearingless slotless slice motor has been reported in [10] to be 115 000 rpm at a circumferential speed of 192.6 m/s, making it suitable for compressor applications.

To further increase the maximum achievable rotational speed, a scaling analysis of such a motor to a smaller size and the associated design procedure were outlined in a previous study [12]. As a proof of concept, the implementation of a motor reaching 150 000 rpm is demonstrated in this work. Its performance is evaluated experimentally based on measured results. Due to the high rotational speed, a potential application area of the presented machine is in optical scanning systems [13].

Pascal Puentener, Marcel Schuck and Johann W. Kolar are with the Power Electronic Systems Laboratory, ETH Zurich, Switzerland. Daniel Steinert and Thomas Nussbaumer are with Levitronix GmbH, Switzerland.
Corresponding author: Pascal Pueuntener, Power Electronic Systems Laboratory, ETH Zurich, Technoparkstrasse 1, 8005 Zurich, Switzerland.
E-mail: puentener@lem.ee.ethz.ch

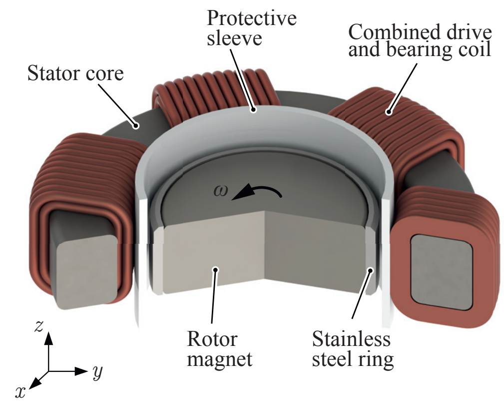

Fig. 1: Topology of the bearingless slotless slice motor.

II. Operating Principle

A. Passive Stability

According to the principle of a bearingless slice motor, the three degrees of freedom of the diametrically-magnetized rotor in axial and tilting directions are passively stabilized [14], [15]. As illustrated in Fig. 2(a), the air gap between the rotor and the inner diameter of the stator core is increased if the rotor is deflected in axial direction or tilted, causing reluctance forces that counteract the displacement. To characterize the bearing properties, the passive stiffnesses in the corresponding directions are specified as

$$c_d = -\frac{\partial F_{\mathrm{b},d}}{\partial d}, \qquad c_q = -\frac{\partial F_{\mathrm{b},q}}{\partial q}, \qquad c_z = -\frac{\partial F_{\mathrm{b},z}}{\partial z}, \tag{1}$$

$$c_\alpha = -\frac{\partial T_{\mathrm{b},\alpha}}{\partial \alpha} \qquad \text{and} \qquad c_\beta = -\frac{\partial T_{\mathrm{b},\beta}}{\partial \beta}, \tag{2}$$

where d and q represent the deflection of the rotor along its direct and quadrature axis, respectively. The angles α and β correspond to tilting around the q- and d-axis, respectively. The rotor needs to be stabilized actively in radial direction.

B. Active Bearing and Drive

Due to the constant air gap length, the magnetic field in the air gap caused by the magnetization of the rotor can be assumed to be ideally sinusoidal and oriented in radial direction

$$\vec{B}_{r\varphi z} \approx B_r \vec{e}_r = \hat{B}_r \cos(\varphi - \vartheta)\vec{e}_r, \tag{3}$$

where ϑ, φ denote the rotor angle and the circumferential variable in cylinder coordinates, respectively.

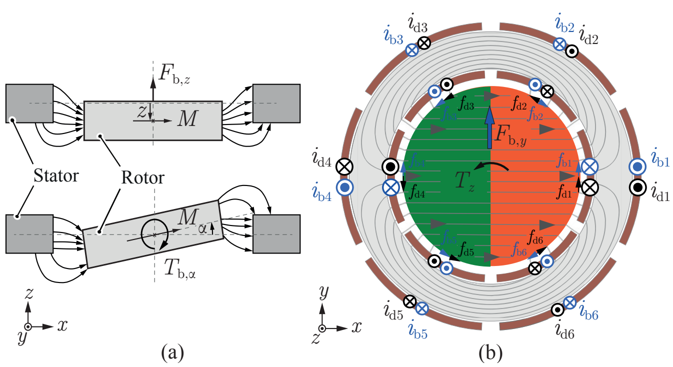

Fig. 2: Stabilizing passive bearing force $F_{\mathrm{b},z}$ due to a deflection in axial direction z and torque $T_{\mathrm{b},\alpha}$ in the tilting direction perpendicular to the direction of magnetization M (a) as well as active torque and force generation in the motor (b).

The Lorentz force acting on the rotor in circumferential direction per unit area can be calculated as

$$\vec{f}_{r\varphi z} = -f_\varphi \vec{e}_\varphi = -A_z \vec{e}_z \times B_r \vec{e}_r, \tag{4}$$

where A_z represents the current surface density of the stator windings, which is the current density times the coil thickness in radial direction, i.e. $A_z = J_z t$. Integration over the cylindrical surface of the rotor results in the total force and torque acting on the rotor

$$\vec{F}_{xy} = h\int_0^{2\pi} \vec{f}\cdot r\,\mathrm{d}\varphi = hR\int_0^{2\pi} f_\varphi \begin{pmatrix} -\sin(\varphi) \\ \cos(\varphi)\end{pmatrix} \mathrm{d}\varphi \tag{5}$$

$$T_z = h\int_0^{2\pi} (\vec{r}\times\vec{f})\cdot r\,\mathrm{d}\varphi = hR^2\int_0^{2\pi} f_\varphi\,\mathrm{d}\varphi, \tag{6}$$

where h, R represent the height and radius of the rotor, respectively.

The drive torque is generated by applying currents of opposite direction to coils which are located on opposite sites of the stator, resulting in a magnetic field with one pole pair. As for any synchronous machine, the driving field needs to be rotated at the same frequency as the rotor. This can be achieved by exciting N equally-distributed coils by the currents

$$i_{\mathrm{d}i} = \hat{I}_{\mathrm{d}i}\cos\left(\frac{(i-1)2\pi}{N} - \vartheta - \varphi_\mathrm{d}\right) \quad i \in \{1, N\}, \tag{7}$$

resulting in a torque

$$T_z = \hat{A}_{z,\mathrm{d}}\hat{B}_r hR^2\pi\cos(\varphi_\mathrm{d}). \tag{8}$$

Bearing forces are obtained by producing a magnetic field with two pole pairs with the phase currents

$$i_{\mathrm{b}i} = \hat{I}_{\mathrm{b}i}\sin\left(2\frac{(i-1)2\pi}{N} - \vartheta - \varphi_\mathrm{b}\right) \quad i \in \{1, N\}, \tag{9}$$

resulting in a Lorentz force

$$\vec{F}_{xy} = \frac{\hat{A}_\mathrm{b}\hat{B}_r hR\pi}{2}\begin{pmatrix}\cos(\varphi_\mathrm{b}) \\ \sin(\varphi_\mathrm{b})\end{pmatrix}. \tag{10}$$

In addition to the Lorentz force, Maxwell forces are caused by the different permeability of the rotor and stator. Considering a sinusoidal distribution of the bearing current surface density

$$\vec{A}_z = \hat{A}_z\sin\left(2\varphi - \vartheta - \varphi_\mathrm{b}\right)\vec{e}_z, \tag{11}$$

the radial component of the generated magnetic flux density lags the phase currents geometrically by $\pi/4$

$$\vec{B}_\mathrm{S} = \hat{B}_\mathrm{S}\sin\left(2\varphi - \vartheta - \varphi_\mathrm{b} + \frac{\pi}{4}\right)\vec{e}_r. \tag{12}$$

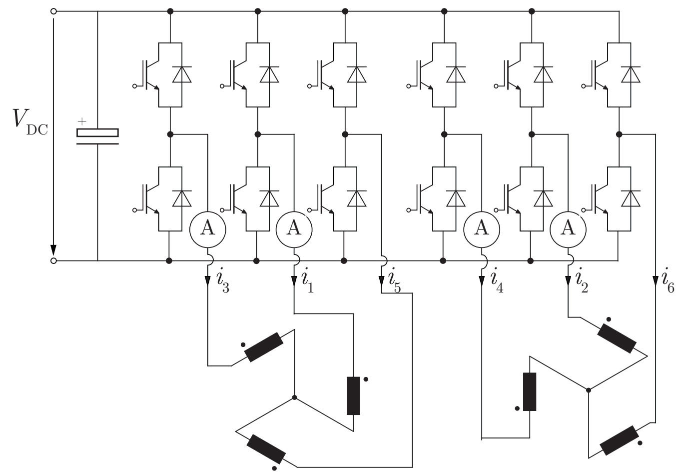

Fig. 3: Circuit diagram of the employed power electronic converter. The switching modules are connected to a dc link voltage of 48 V and are operated at a switching frequency of 21 kHz. The coils are depicted as arranged in the motor.

The air gap field is strengthened on one side of the rotor and weakened on the other. The resulting Maxwell force is added to the Lorentz force [11].

The two aforementioned cases of active torque and radial bearing force generation are depicted in Fig. 2(b) together with the corresponding drive currents (black) and bearing currents (blue). An exemplary current excitation to generate a force in y-direction is shown (i.e. $\varphi_\mathrm{b} = 90°$). The magnetic flux lines as generated by the permanent magnetization of the rotor only have been added to the figure.

In a system with combined windings, such as the motor presented here, the coils carry both bearing and drive currents. Consequently, a drive torque and radial bearing forces can be generated using the same coils [16]. Following the notation of Fig. 2(b), the currents can be written as

$$i_1 = i_{\mathrm{b}1} + i_{\mathrm{d}1} \qquad i_4 = i_{\mathrm{b}1} - i_{\mathrm{d}1} \tag{13}$$

$$i_2 = i_{\mathrm{b}2} + i_{\mathrm{d}2} \qquad i_5 = i_{\mathrm{b}2} - i_{\mathrm{d}2} \tag{14}$$

$$i_3 = i_{\mathrm{b}3} + i_{\mathrm{d}3} \qquad i_6 = i_{\mathrm{b}3} - i_{\mathrm{d}3}, \tag{15}$$

where the subscripts b and d denote bearing currents and drive currents, respectively. As

$$i_1 + i_3 + i_5 = 0 \quad \text{and} \quad i_2 + i_4 + i_6 = 0 \tag{16}$$

hold, the coils can be connected to the supplying power electronic converter as two three phase systems with floating star points, as shown in Fig. 3. A more detailed explanation can be found in [11].

III. Prototype of the High Speed Motor

The design parameters and components of the implemented motor prototype are described in this section. A more detailed analysis of possible designs as well as the optimization of the passive and active motor properties is outlined in [12]. Figure 4 shows an annotated photograph of the implemented high speed slotless slice motor and Table I summarizes the relevant dimensions and parameters.

A. Stator

The six coils are wound toroidally around the ring-shaped stator core. The latter is manufactured from Metglas 2605SA1

This is the author's version of an article that has been published in this journal. Changes were made to this version by the publisher prior to publication.
The final version of record is available at http://dx.doi.org/10.1109/TMECH.2018.2873894

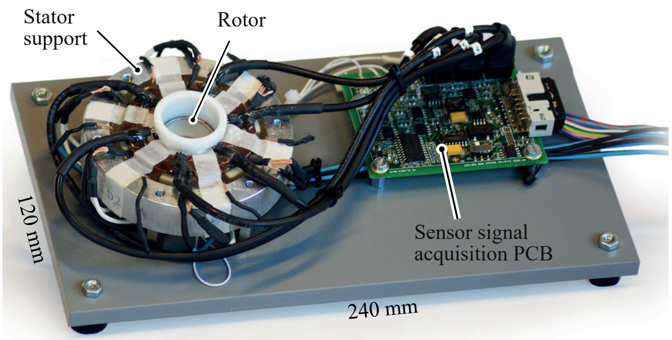

Fig. 4: Photograph of the implemented prototype. The depicted sensor signal acquisition printed circuit board (PCB) processes the measured signals prior to transmission to the motor controller.

amorphous alloy material as it features lower core losses than conventional sheeted electrical steel, especially at the targeted high field frequencies [17]. To achieve a high tilting stiffness and, therefore, a better rotor stability, the rotor to stator height ratio is chosen to be 1.125 according to [12]. The drive and bearing coils consist of 21 windings each. To reduce proximity- and skin-effect-related losses, the coils are wound using Litz wire with a cross sectional copper area of 0.255 mm^2.

B. Rotor

The rotor consists of a diametrically-magnetized NdFeB permanent magnet with a diameter of 20 mm. To protect the brittle material against mechanical damage, it is encapsulated by a stainless steel with a wall thickness of 1 mm (cf. Fig. 1).

Due to the disc shape, this rotor can withstand higher mechanical stresses than the ones with a center hole which were tested in previous publications [10]. The maximum stress occurs at the center of the disc and can be calculated as

$$\sigma_{\max} = (3+\nu)\frac{\rho v^2}{8}, \tag{17}$$

where ρ, ν, v denote the density of the rotor material, its Poisson's ratio and the circumferential speed, respectively [18]. According to the datasheet provided by the manufacturer ($\sigma_\mathrm{s} = 80\,\mathrm{MPa}$, $\rho = 7\,500\,\mathrm{kg/m^3}$, $\nu = 0.24$), the maximum achievable peripheral speed is given as

$$v_{\max} = \sqrt{\frac{8\sigma_\mathrm{s}}{(3+\nu)\rho}} = 162\,\mathrm{m/s}, \tag{18}$$

where σ_s is the tensile strength of the material. For the given diameter, this corresponds to a rotational speed of $n_{\max} = 155\,000\,\mathrm{rpm}$.

C. Control Structure

The control of the active magnetic bearing is implemented by a cascaded PID position controller with an underlying PI current controller. The reference bearing currents are calculated based on the difference between the reference position and radial displacement of the rotor. They are then compared to phase current measurements as shown in Fig. 3. The current controller then sets the duty cycles of the PWM-modulated half bridges accordingly. Field oriented control is applied for the bearing as well as the drive currents. The rotational speed is governed by a PI controller. A detailed description of the control structure and further explanations can be found in [19].

TABLE I: Dimensions of the Prototype

Parameter	Value	Unit
rotor magnet diameter	20	mm
rotor outer diameter	22	mm
rotor height	9	mm
rotor mass	26	g
stator outer diameter	41	mm
stator height	8	mm
protective sleeve thickness	0.8	mm
stainless steel ring thickness	1	mm
magnetic air gap	4.5	mm
mechanical air gap	0.6	mm
torque constant	23.2	mNm/A
bearing constant	1.48	N/A
tilting stiffness c_α around d	0.95	mNm/deg
tilting stiffness c_β around q	2.1	mNm/deg
axial stiffness c_z	2.26	N/mm
coil resistance	112	mΩ
coil inductance	25.6	µH
number of turns per winding	112	–
maximum input power	600	W

IV. Performance Evaluation of the Motor

A. Acceleration and Maximum Speed

To test the performance of the motor, the rotor was accelerated from standstill to 150 000 rpm. Trace (a) of Fig. 5 shows the Hall sensor signal, which is used to determine the rotor angle, during such a speedup. Its frequency is directly proportional to the rotational speed. The magnitude of the signal is decreased with increasing rotational speed due to the employed low-pass filter, which is necessary to suppress high frequency noise. The maximum speed of 150 000 rpm is reached after 2.3 s, corresponding to an acceleration of 65 000 rpm/s. A detailed view of the measurements at maximum speed is shown in the lower part of Fig. 5. The motor requires an RMS phase current of 5.3 A to overcome the motor losses and to stabilize the rotor (b). The position signals (c) and (d) show that the rotor deviates at most 240 µm from its center position and that no significant signal component is present at the rotational frequency, indicating that the rotor is sufficiently well balanced. The axial rotor displacement was measured using a laser distance sensor to be in the range of 20 µm at maximum speed (e). The maximum achieved frequency is 2 500 Hz, corresponding to a rotational speed of 150 000 rpm, as shown in the flux signal measured by a Hall sensor (f). Higher speeds have not been tested to avoid destruction of the rotor due to excessive centrifugal loading.

The aforementioned deflections of the rotor from its equilibrium position are sufficiently low to allow for stable operation of the motor over the entire speed range and high repeatability of the results. If decreased vibrations of the rotor are required for the intended application, such as in high precision optical scanning system, this can be achieved by more accurate vibration control. Due to the high passive axial stiffness (see Table I), stable levitation of the rotor is possible for an additional axial load of up to 800 g ($\approx$ 30 times the rotor mass). An axial force of 12 N is required to completely remove the rotor from the stator bore.

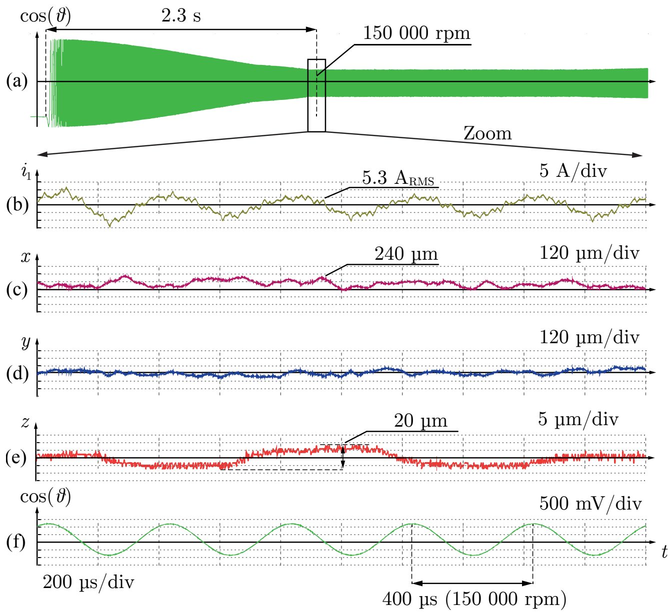

Fig. 5: Flux signal during speedup (a) as well as exemplary phase current (b), radial position signals (c) and (d), axial deflection (e), and Hall sensor signal (f) at the maximum speed of 150 000 rpm.

B. Losses

To examine the motor losses, the rotor was levitated and its rotational speed was increased in steps of 10 000 rpm. Measurements were taken once the steady state at the desired rotational speed had been reached.

The overall motor losses P_{mot} were measured at the output of the controller. To do so, four phase currents and the corresponding voltages were measured using a Yokogawa WT1804E high precision power analyzer. The overall losses were calculated from the measurements as

$$P_{\mathrm{mot}} = \overline{u_{13} i_1} + \overline{u_{53} i_5} + \overline{u_{24} i_2} + \overline{u_{64} i_6}, \tag{19}$$

where the indices denote the respective phase of the motor.

The occurring copper losses P_{cu} were calculated using the measured phase currents and the corresponding resistances R_n as

$$P_{\mathrm{cu}} = \sum_{n=1}^{6} R_n I_{\mathrm{rms},n}^2. \tag{20}$$

To identify the windage losses P_{wind}, the aforementioned measurements were repeated over the entire speed range with the rotor being spun in vacuum at a pressure of ≤ 4 mbar. Due to the small radius R of the rotor, these losses are expected to be small, as their dependency on the radius is given by

$$P_{\mathrm{wind,rad}} \propto \omega^3 R^4 \quad \text{and} \quad P_{\mathrm{wind,ax}} \propto \omega^3 R^5, \tag{21}$$

where $P_{\mathrm{wind,rad}}$, $P_{\mathrm{wind,ax}}$ are the air friction losses caused by the cylindrical surface and the top and bottom faces of the rotor, respectively [20].

The remaining losses $P_{\mathrm{hys,ec}}$ are composed of hysteresis losses P_{hys} in the stator core and eddy current losses P_{ec} in the stator and the rotor.

Figure 6 shows the obtained losses from standstill up to 150 000 rpm. As the rotational speed is increased, hysteresis and eddy current losses begin to grow and constitute the dominant part of the total losses. Due to the low resistance of the stator windings, the copper losses remain small throughout a wide speed range. Above 120 000 rpm these losses increase rapidly due to the increasing current ripple caused by the limited switching frequency of the power electronic converter. The ripple at 150 000 rpm has been visualized for an exemplary phase current in the inset of Fig. 6. As it adds significant harmonic content to the stator field, it also causes an increase of $P_{\mathrm{hys,ec}}$.

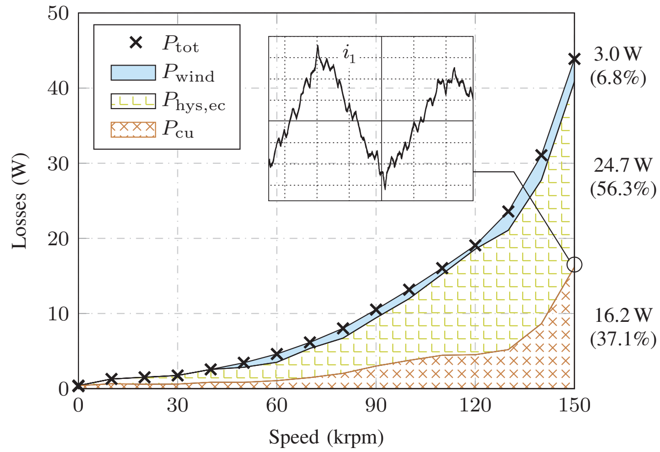

Fig. 6: Measured motor over the entire speed range. The inset shows a detailed view of an exemplary phase current at maximum speed.

At 150 000 rpm the losses sum up to 43.9 W, with $P_{\mathrm{hys,ec}}$ constituting 56.3 % (24.7 W) of the overall losses. The copper losses and windage losses amount for 37.1 % (16.2 W) and less than 7 % (3 W), respectively. The latter have a minor contribution, as expected. Detailed loss investigations of slotless bearingless drives including the respective theoretical models can be found in [21], [22].

V. Conclusion

Based on the conceptional study outlined in [12], a prototype of a bearingless slotless slice motor for high rotational speeds was designed, implemented and tested successfully. The rotor is levitated stably over the entire speed range up to its maximum rotational speed of 150 000 rpm. Due to its solid disc shape, the brittle material is able to withstand the occurring mechanical stress and allows for repeatable experiments. The maximum speed reported in this work was achieved reproducibly and under stable operating conditions. Measurements of the motor losses have shown that these are mainly due to iron and copper losses, while windage losses remain small. To the knowledge of the authors, the rotational speed as demonstrated in this work is the highest rotational speed attained by a bearingless slice motor to date.

References

[1] T. Baumgartner, R. Burkart, and J. W. Kolar, "Analysis and design of an ultra-high-speed slotless self-bearing permanent-magnet motor," in *Proc. IECON 2012 - 38th Annual Conf. IEEE Industrial Electronics Society*, Oct. 2012, pp. 4477–4483.

[2] A. Chiba, T. Fukao, O. Ichikawa, M. Oshima, M. Takemoto, and D. G. Dorrell, *Magnetic bearings and bearingless drives*. Elsevier, 2005.

[3] E. Hou and K. Liu, "Tilting characteristic of a 2-axis radial hybrid magnetic bearing," *IEEE Transactions on Magnetics*, vol. 49, no. 8, pp. 4900–4910, Aug 2013.

[4] R. Schoeb and N. Barletta, "Magnetic bearing. Principle and application of a bearingless slice motor." *JSME International Journal Series C Mechanical Systems, Machine Elements and Manufacturing*, vol. 40, no. 4, pp. 593–598, 1997.

[5] B. Warberger, R. Kaelin, T. Nussbaumer, and J. W. Kolar, "50- /2500-W bearingless motor for high-purity pharmaceutical mixing," *IEEE Transactions on Industrial Electronics*, vol. 59, no. 5, pp. 2236–2247, May 2012.

[6] T. Nussbaumer, K. Raggl, P. Boesch, and J. W. Kolar, "Trends in integration for magnetically levitated pump systems," in *Proc. Power Conversion Conf. - Nagoya PCC '07*, Apr. 2007, pp. 1551–1558.

[7] J. Asama, T. Fukao, A. Chiba, A. Rahman, and T. Oiwa, "A design consideration of a novel bearingless disk motor for artificial hearts," in *2009 IEEE Energy Conversion Congress and Exposition*, Sept 2009, pp. 1693–1699.

[8] R. Schoeb, N. Barletta, A. Fleischli, G. Foiera, T. Gempp, H. Reiter, V. L. Poirier, D. B. Gernes, K. Bourque, H. M. Loree *et al.*, "A bearingless motor for a left ventricular assist device (lvad)," in *Seventh International Symposium on Magnetic Bearings, Zurich, Switzerland*, 2000, pp. 383–88.

[9] N. Boules, "Impact of slot harmonics on losses of high-speed permanent magnet machines with a magnet retaining ring," *Electric Machines and Electromechanics*, vol. 6, no. 6, pp. 527–539, 1981.

[10] H. Mitterhofer, W. Gruber, and W. Amrhein, "On the high speed capacity of bearingless drives," *IEEE Transactions on Industrial Electronics*, vol. 61, no. 6, pp. 3119–3126, Jun. 2014.

[11] D. Steinert, T. Nussbaumer, and J. W. Kolar, "Slotless bearingless disk drive for high-speed and high-purity applications," *IEEE Transactions on Industrial Electronics*, vol. 61, no. 11, pp. 5974–5986, Nov 2014.

[12] D. Steinert, T. Nussbaumer, and J. W. Kolar, "Concept of a 150 krpm bearingless slotless disc drive with combined windings," in *Electric Machines Drives Conference (IEMDC), 2013 IEEE International*, May 2013, pp. 311–318.

[13] G. F. Marshall and G. E. Stutz, *Handbook of optical and laser scanning*. CRC Press, 2011.

[14] W. Gruber, "Bearingless slice motors: General overview and the special case of novel magnet-free rotors," in *Innovative Small Drives and Micro-Motor Systems; 9. GMM/ETG Symposium*, Sept 2013, pp. 1–6.

[15] D. Steinert, T. Nussbaumer, and J. W. Kolar, "Evaluation of one-and two-pole-pair slotless bearingless motors with toroidal windings," *IEEE Transactions on Industry Applications*, vol. 52, no. 1, pp. 172–180, 2016.

[16] K. Raggl, J. W. Kolar, and T. Nussbaumer, "Comparison of winding concepts for bearingless pumps," in *Proc. 7th Internatonal Conf. Power Electronics*, Oct. 2007, pp. 1013–1020.

[17] *2605SA1 Magnetic Alloy*, Metglas, 4 2011.

[18] E. J. Hearn, *Mechanics of Materials 2: The mechanics of elastic and plastic deformation of solids and structural materials*. Butterworth-Heinemann, 1997.

[19] B. Warberger, T. Reichert, T. Nussbaumer, and J. W. Kolar, "Design considerations of a bearingless motor for high-purity mixing applications," in *SPEEDAM 2010*, June 2010, pp. 1454–1459.

[20] A. Borisavljevic, *Electromagnetic Modeling of Slotless PM Machines*. Berlin, Heidelberg: Springer Berlin Heidelberg, 2013, pp. 29–70.

[21] H. Mitterhofer, D. Andessner, and W. Amrhein, "Analytical and experimental loss examination of a high speed bearingless drive," in *International Symposium on Power Electronics Power Electronics, Electrical Drives, Automation and Motion*, June 2012, pp. 146–151.

[22] D. Steinert, I. Kovacevic-Badstübner, T. Nussbaumer, and J. W. Kolar, "Loss investigation of slotless bearingless disk drives," in *2015 IEEE Energy Conversion Congress and Exposition (ECCE)*, Sept 2015, pp. 4418–4424.

Pascal Püntener (S'15) was born in Erstfeld, Switzerland, in 1989. He studied mechanical and process engineering at the Swiss Federal Institute of Technology Zurich (ETH Zurich), Zurich, Switzerland, where he focused on dynamics and control theory. He carried out his master thesis in cooperation with an industry partner on robust control of a plant with uncertain resonance. After receiving his MSc degree in October 2015, he joined the Power Electronic Systems Laboratory as a PhD student.

Marcel Schuck (S'13-M'18) received the B.Sc. degree in Electrical and Computer Engineering from the Technische Universität Darmstadt, Germany, in 2011 and the M.Sc. degree in the same field from the University of Illinois at Urbana-Champaign in 2013. He received an MBA degree from the Collège des Ingénieurs in Paris, France in 2014. He was a Ph.D. student at the Power Electronic Systems Laboratory at ETH Zurich, Switzerland from 2014 to 2017, where he is currently working as a postdoctoral researcher. His research interests include ultra-high speed bearingless machines, acoustic levitation, and mechatronic systems.

Daniel Steinert (S'13) was born in Roth, Germany, in 1987. He received the M.Sc. degree in mechatronics from Dresden University of Technology, Dresden, Germany, in 2012, where he focused on micromechatronics and precision engineering. In 2015, he received the Ph.D. degree from the Power Electronic Systems Laboratory of the Swiss Federal Institute of Technology Zurich (ETH Zurich), Zurich, Switzerland, where he worked on high-speed bearingless motors. He is currently with Levitronix GmbH, Zurich, Switzerland, where his research is focused on bearingless motor topologies, control concepts, losses, and applications of bearingless motors.

Thomas Nussbaumer (S'02-M'06) was born in Vienna, Austria, in 1975. He received the M.Sc. (Hons.) degree in electrical engineering from Vienna University of Technology, Vienna, in 2001 and the Ph.D. degree from the Swiss Federal Institute of Technology Zurich (ETH Zurich), Zurich, Switzerland, in 2004. From 2001 to 2006, he was with the Power Electronic Systems Laboratory, ETH Zurich, where he was involved in research on modeling, design, and control of three-phase rectifiers, power factor correction techniques, and electromagnetic compatibility. Since 2006, he has been with Levitronix GmbH, Zurich, where he is currently involved in research on bearingless motors, magnetic levitation, and permanent-magnet motor drives for the semiconductor and biotechnology industry. His current research is focused on compact and high-performance mechatronic systems, including novel power electronics topologies, control techniques, drive systems, sensor technologies, electromagnetic interference, and thermal aspects.

Johann W. Kolar (S'89-M'91-SM'04-F'10) received the M.Sc. and Ph.D. degrees (summa cum laude) from Vienna University of Technology, Vienna, Austria. He is currently a Full Professor with and the Head of the Power Electronic Systems Laboratory, Swiss Federal Institute of Technology Zurich (ETH Zurich), Zurich, Switzerland. He has proposed numerous novel pulsewidth-modulation converter topologies and modulation and control concepts, published more than 650 scientific papers in international journals and conference proceedings, and filed more than 110 patents. The focus of his current research is on ultracompact and ultraefficient converter topologies employing latest power semiconductor technology (SiC and GaN), wireless power transfer, solid-state transformers, power supplies on chip, and ultra-high speed and bearingless motors. Prof. Kolar was a recipient of 21 IEEE TRANSACTIONS and conference prize paper awards, the 2014 SEMIKRON Innovation Award, the 2014 IEEE Power Electronics Society R. David Middlebrook Award, and the ETH Zurich Golden Owl Award for Excellence in Teaching.